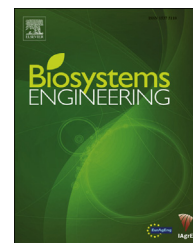


Available online at [www.sciencedirect.com](http://www.sciencedirect.com)

ScienceDirect

journal homepage: [www.elsevier.com/locate/issn/15375110](http://www.elsevier.com/locate/issn/15375110)

## Special Issue: Innovations in Medicine and Healthcare

## Research Paper

## A web-based framework for anatomical assessment of the retina using OCT

Ana González-López <sup>a,\*</sup>, Marcos Ortega <sup>a</sup>, Manuel G. Penedo <sup>a</sup>,  
Pablo Charlón <sup>b</sup><sup>a</sup> Departamento de Computación, Universidade da Coruña, Spain<sup>b</sup> Sociedad Gallega de Optometría Clínica, Spain

## ARTICLE INFO

## Article history:

Published online 23 April 2015

## Keywords:

Medical informatics applications

Web interface

Optical coherence tomography  
(OCT)

Retinal layers

Segmentation

Active contours

Optical Coherence Tomography (OCT) is a clinical standard imaging technique in ophthalmology, which provides much more information than other classical modalities. Since retinal morphology and pathological structures can be identified in an effective way in the OCT images, image processing-based methods are emerging to extract their information. As a prior step to any automatic application for feature extraction, delimitation of retinal layers must be automated. On the other hand, medical research needs to process a large amount of information from different patients and the clinical studies are usually performed in a multi-centre schema. Therefore, not only is automation of retinal layer segmentation needed, but also a flexible framework must be designed to allow the experts to manage all clinical data, as well as extracting features of interest. With that aim, this work presents a framework for OCT image processing, which provides automatic procedures for retinal layer segmentation and the extraction of different statistics for medical support. A web-based interface was designed in order to make it available to the ophthalmic experts and accessible from different centres. Since the framework was used by ophthalmologists in a real case scenario, its robustness and suitability for this task are shown, making it a very relevant tool for clinical and research purposes.

© 2015 IAGRE. Published by Elsevier Ltd. All rights reserved.

## 1. Introduction

In ophthalmology, retinal analysis is a key field for the early diagnosis of several diseases. Optical Coherence Tomography (OCT) has become an essential imaging technique for ophthalmic specialists, because it is a non-invasive, contact-

less method that provides a cross sectional image of the retina and its structures in a real time fashion (Puzeyeva et al., 2011). Retinal morphology can be identified effectively in these images, allowing disease pathogenesis and progression to be observed. OCT-techniques have progressed in recent years, especially since the appearance of spectral-domain (SD) OCT. This modality presents a great potential for clinical

\* Corresponding author. Fac. Informática, Campus de Elviña s/n, A Coruña 15071, Spain. Tel.: +34 981 167 000 1330.

E-mail addresses: [ana.gonzalez@udc.es](mailto:ana.gonzalez@udc.es) (A. González-López), [mortega@udc.es](mailto:mortega@udc.es) (M. Ortega), [mgpinedo@udc.es](mailto:mgpinedo@udc.es) (M.G. Penedo), [pcharlon@sgoc.es](mailto:pcharlon@sgoc.es) (P. Charlón).

<http://dx.doi.org/10.1016/j.biosystemseng.2015.04.001>

1537-5110/© 2015 IAGRE. Published by Elsevier Ltd. All rights reserved.

Nomenclature			
$\alpha$	Weight of the internal energy term $v_s$	$I_t$	External energy term used to segment ILM, encouraging areas located at the top part in the image $I$
$\beta$	Weight of the internal energy term $v_{ss}$	$m_{ci}$	Range of rows explored around the each node in RPE/C to find the best projection $c'$ of $c \in C$
$\gamma$	Weight of the internal energy term $v_{ss_{nhb}}$	$n_s$	Number of steps used to adjust the active contour
$\epsilon$	Weight of the external energy term $I_t$	$n_{ac}$	Number of nodes in the active contour
$C$	Set of curves generated for I/RPE and RPE/C refinement	$n_{nhb}$	Neighbourhood size used to calculate $v_{ss_{nhb}}$
$c'$	Projection of a curve $c \in C$ over a boundary	$nc_{min}$	Number of points used to generate curves in $C$
$d_{cl}$	Distance between a curve in $C$ and a layer boundary	$u_1$	Weight of the external energy term $I_i$
$d_{cni}$	Distance between a curve in $C$ and a node $n_i$ , used as fitness measure	$u_2$	Weight of the external energy term $I_g$
$d_g$	Distance between a curve in $C$ and both I/RPE and RPE/C boundaries	$v_{ss_{nhb}}$	Extended second order internal energy term
$E_{ext}$	External energy of the active contour	$v_{ss}$	Second-order internal energy term
$E_{int}$	Internal energy of the active contour	$v_s$	First-order internal energy term
$E_{total}$	Global energy of the active contour	$vec$	Vector containing the mean intensity along each image column
$I$	First image considered in the computation of the external energy	$vec_{med}$	Median value computed over blurred $vec$
$I'$	Second image considered in the computation of the external energy	$vec_{std}$	Standard deviation computed over blurred $vec$
$I'_e$	External energy term representing the edges in the image $I'$	$w_1$	Weight of the external energy term $I'_{gi}$
$I'_{gi}$	External energy term representing the intensity of the area above the current pixel in the image $I'$	$w_2$	Weight of the external energy term $I'_g$
$I'_{maxg}$	External energy term representing the gradient distance to the strongest edges in the image $I'$	$w_3$	Weight of the external energy term $I'_e$
$I_g$	External energy term defined as gradient distance computed over the image $I$	$w_4$	Weight of the external energy term $I'_{maxg}$
$I_i$	External energy term defined as the intensity at the current pixel in the image $I$	EZPR	External Zone of Photoreceptors
		I/RPE	Boundary determined by the Retinal Pigment Epithelium-Bruch's Complex and the Interdigitation
		ILM	Top boundary of the Internal Limiting Membrane
		M/E	Boundary determined by the Myoid and the Ellipsoid
		RPE/C	Boundary determined by the Retinal Pigment Epithelium-Bruch's Complex and the Choroid

ophthalmology due to its extremely high sensitivity and image-acquisition speed, both essential characteristics for ophthalmic applications (Yaqoob, Wu, & Yang, 2005).

OCT retinal analysis allows several diseases to be diagnosed: OCT layer-thickness information is useful in diagnosing eye diseases like macular degeneration (Keane et al., 2012), glaucoma (Bowd, Weinreb, Williams, & Zangwill, 2000) and diabetic retinopathy (Sanchez-Tocino, Alvarez-Vidal, Maldonado, Moreno-Montañes, & Garcia-Layana, 2002). On the other hand, retinal thinning is correlated with multiple sclerosis (Albrecht et al., 2012) and Parkinson's disease (Tian, Zhu, & Liu, 2011). Therefore, delimitation of retinal layers is essential for ophthalmology experts. Since manual delimitation is a very tedious, time-consuming task, automatic image processing-based methods have become more and more popular, allowing relevant information to be extracted from these images in an easy and fast manner. With that aim, an automated framework to segment retinal layers in OCT images is proposed in this work.

Retinal layer segmentation is a widely studied problem. Different approaches can be found in previous works: Graph-based techniques have been presented by Haeker et al. (2007), Garvin et al. (2009), Lee et al. (2010) and Kafieh, Rabbani, Abràmoff, and Sonka (2013), which transform the segmentation task into that of finding the minimum-closed-set in a

geometric graph. A further step with graph-based methods was introduced by Antony et al. (2010), where the layer segmentation is performed in OCT images centred on the optic nerve head. Dynamic programming was incorporated by Chiu et al. (2010), while the method proposed by Yang et al. (2011) combines local and global gradient information to tackle a shortest-path-based segmentation in order to build layer thickness maps for pathological patients.

Other works consider active contours for this task: Yazdanpanah, Hamarneh, Smith, and Sarunic (2011) present a semiautomatic method to segment retinal layers, while the active contour traditional model was extended by Mishra, Wong, Bizheva, and Clausi (2009) to conform a two-step kernel-based optimisation process to segment rat retinal layers. Since in that method, the segmentation process is fast and results presents appropriate accuracy and high smoothness, this work intends to take advantage of these properties to segment retinal layers. Thus, an active contour-based technique is designed to segment retinal layers considered in this work. This method does not only segment layers when they are appreciable, but also when vessel shades are present, layers have suffered alterations or are absent in certain parts of the retina, making it robust enough for clinical use.

However, it is necessary to take into account that in the medical field, a collaborative environment is essential, given

that studies are usually performed by several experts in different centres. In this context, a web-based framework seems suitable. This kind of image processing-based applications has been introduced in several medical fields, such as in magnetic resonance imaging of the brain (Karsch, Grinstead, He, & Duan, 2008) and screening for skin cancer (Blackledge & Dubovitski, 2011). In ophthalmology, most systems are focused on retinal analysis in fundus images: a web-based system for screening was used by Abramoff and Suttorp-Schulten (2005) to detect diabetic retinopathy over a considerable population, while the framework proposed by Ortega et al. (2010) allows a retinal analysis on fundus images to be performed automatically, extracting useful indicators for diagnosis, such as the arteriolar-to-venular (AVR) ratio. However, to the best of our knowledge, there are no previous web-based systems for OCT image processing. With that aim, a web-based interface is designed in this work, in order to make the layer segmentation method available to the experts. Other automated modules are also integrated in the application, such as the extraction of statistical indicators, useful to perform clinical studies. Thus, a complete and powerful tool for researching purposes is presented.

This paper is organised as follows: firstly, a general overview of the framework is presented in Section 2. In Section 3, both layer segmentation and statistics extraction services included in the application are described in detail. Since expert assessment is essential to show the robustness of this work, results are presented in Section 4. Finally, Section 5 presents conclusions and future lines of research.

## 2. Framework

The goal of this work is developing a generic framework to process OCT retinal images, with the purpose of extracting relevant indicators for diagnosis-support. Main requirements considered in designing this system are the following: it must detect automatically the retinal layers and compute several parameters from OCT retinal images in a repeatable and objective manner, as well as being usable by different users with basic computer skills from different locations. Besides that, integration of new image processing modules should be easy, with the purpose of enabling the extension of the system in the future with new capabilities.

In order to obtain a framework satisfying all these characteristics, different modules were developed and a web interface was designed to allow the specialists to interact with them.

### 2.1. Web interface

Although standalone applications are easy to built based on previous image processing methods, this kind of applications presents three main disadvantages in relation to the main requirements of this project:

- Data is computed and stored in each user's computer.
- The application is dependent on the user's platform (Windows, Linux, Mac).

- Application upgrades require that all the users update their software.

In contrast to standalone applications, web applications run on a server, so that both the software and the data are centralised in one location. The user (client) makes requests to the web server and receives data via a web browser. This implies two benefits: firstly, the application is accessible from any location or platform and then, specific software need not be installed to run services provided by the web application. In this context, the framework consists of an application composed of several automatic modules and a web interface, which is developed for the tool in order to provide the required characteristics.

The web interface was implemented using PHP, HTML, CSS and JavaScript. Apache Tomcat was used as the web server and MySQL as the relational database. Figure 1 shows the architecture of this framework.

Regarding the functionalities provided by this framework, authentication is required from the users and then they can make use of a management module. This module includes different functionalities, such as storage of relevant patient data (code, age ...) or searching utilities (filtered by patient age, pathology ...).

Besides these capabilities, since the aim of this application is processing OCT images with the purpose of diagnosis-support, the framework integrates some modules with image processing tools.

### 2.2. Image processing tools

Both proposed services, the automatic detection of retinal layers and measuring features of interest, are integrated in some libraries of OCT retinal image processing. They have been developed in C++ due to its efficiency and use common image processing libraries such as OpenCV. These services are explained deeply in Section 3.

## 3. OCT retinal image processing services

As commented previously, layer delimitation is a tedious task when done manually and so as is the computation of statistical indicators from the OCT images. For ophthalmology experts, it is essential to count on an automatic tool to extract this information from the OCT images. For that purpose, two

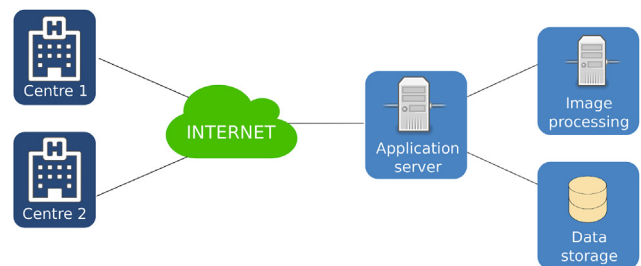


**Fig. 1 – Overview of the proposed framework: several ophthalmology-support systems request data from the application server via HTTP.**

modules have been designed and integrated with the web interface. The first module performs the layer segmentation over the OCT images, while the second one allows indicators that are useful for the experts to be computed from the data.

### 3.1. Layer Segmentation Service

Current scanners provide an OCT cube, which consists of a sequence of cross-sectional images of the retina. Since in this context, the OCT cube is composed of 128 images and the segmentation is performed for each of them separately, the service works in an off-line mode. However, the on-line service is being designed at the moment with the purpose of being integrated in the framework soon. Thus, once the user selects which layer boundaries must be segmented, they are detected over all images in the OCT cube and can be used later to extract the desired statistical information using the service described in Section 3.2.

In particular, four layer boundaries are considered in this work. They are shown in Fig. 2: Internal Limiting Membrane (ILM) and borderline between the Retinal Pigment Epithelium-Bruch's Complex with the Choroid (RPE/C) are segmented, because they correspond to limits of the retina; then, top boundaries of the Ellipsoid (delimited by the Myoid) and Retinal Pigment Epithelium-Bruch's Complex are detected (they will be referenced as M/E and I/RPE boundaries in the following text), since they bound the External Zone of Photoreceptors (EZPR). This zone, marked in Fig. 2, includes Ellipsoid, Outer Segments and Interdigitation layers, which are strongly correlated with retinal sensitivity in pathological patients (Yohannan et al., 2013) or visual recovery after surgery (Itoh, Inoue, Rii, Hirota, & Hirakata, 2013), as well as providing a prognostic factor for some surgeries (Shiono et al., 2013). Since several ophthalmological studies are focused on EZPR, automating its detection seems relevant.

Segmentation of these layer boundaries is performed through a four-stage process, as Fig. 3 shows graphically. Firstly, ILM is segmented and the area of the fovea can be located roughly using several frames, because it corresponds to a hollow in that layer. After segmenting RPE/C and M/E, I/RPE is detected.

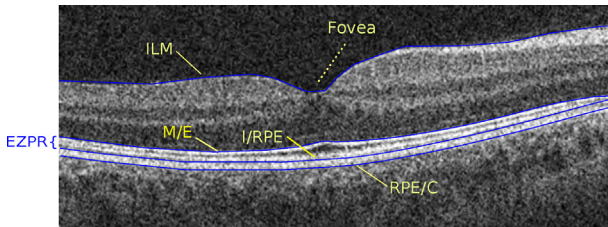


**Fig. 2 – Sample OCT image marked with the retinal layers considered in this work: top boundary of the Internal Limiting Membrane (ILM), borderline between the Myoid and Ellipsoid (M/E) and both boundaries of the Retinal Pigment Epithelium-Bruch's Complex, delimited by the Interdigitation (I/RPE) and the Choroid (RPE/C), respectively. The External Zone of Photoreceptors (EZPR) is delimited by M/E and I/RPE.**

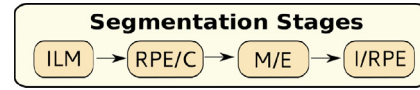


**Fig. 3 – Phases in the global method: firstly, top boundary of the Internal Limiting Membrane (ILM) is detected; then, borderline between the Retinal Pigment Epithelium-Bruch's Complex and the Choroid (RPE/C) is segmented; once the boundary of the Myoid with the Ellipsoid (M/E) has been obtained, boundary between Interdigitation and Retinal Pigment Epithelium-Bruch's Complex (I/RPE) can be detected.**

The process used to segment a particular boundary is composed of two steps: in the preprocessing, the region of interest is bounded and then, an active contour-based process is performed. Although results provided by this method are very promising, some refinement can be included in order to improve inaccurate segmentation caused by the presence of alterations and the lack of information. This refinement process is proposed in Section 3.1.3: firstly, M/E is improved and then, a simultaneous refinement combining information of both RPE boundaries is designed to achieve a better adjustment.

#### 3.1.1. Preprocessing

This step determines the region of interest (ROI) in which the searching must be done. Firstly, the input image is processed to enhance contrast and blurred to remove noise. After that, for ILM and RPE/C boundaries, the image is binarised using a threshold which depends on the intensity distribution in the image; then, the morphological operator of closing is used to fill holes and erase spurious groups of pixels; finally, the active contour can be initialised based on the pixels that remains in each column, because these boundaries (ILM and RPE/C) correspond to the upper/lower limits of the binarised region; thus, these limits are extracted and fitted to a curve in order to obtain a smooth initial contour. Therefore, the ROI can be determined by a wide area surrounding this initial contour.

Figure 4 presents this process for a sample image. With regards to M/E and I/RPE, the active contour initialisation and ROI bounding are done based on the previous boundaries.

#### 3.1.2. Active contour model-based segmentation

Boundary segmentation is based on active contours (Kass, Witkin, & Terzopoulos, 1988), which are energy-minimising splines guided by external and internal forces that pull the segmentation towards features in the image. External forces attract the contour to the desired features in the image, whereas model behaviour (curvature, continuity) is governed by internal forces:

$$E_{total} = \int E_{int}(v(s)) + E_{ext}(v(s))ds \quad (1)$$

In this work, topology is defined as a linear sequence of equidistant  $n_{ac}$  nodes. Each node corresponds to one pixel in the image, connected to two neighbours, except for the first and the last ones. A greedy approach is used for experiments in this work.



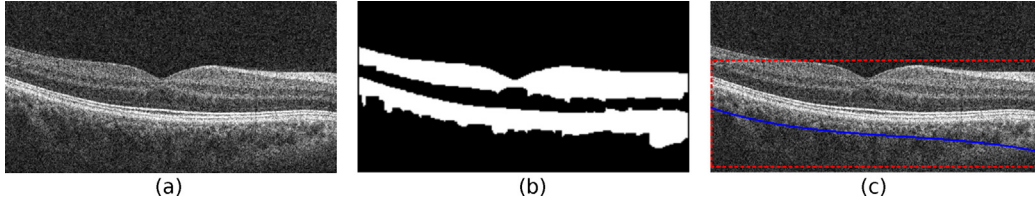


**Fig. 4 – Initialisation of the active contour: (a) original image; (b) image after thresholding and morphological operators; (c) initialisation of the contour as the curve-fitted lower boundary of the binarised area, determining the ROI in red square.**

Regarding internal forces, curve behaviour is modelled using first and second-order terms, represented by  $v_s(s)$  and  $v_{ss}(s)$ . The second order term is extended to consider a neighbourhood  $n_{nhb}$  in order to encourage curvature continuity, reflected in a new term  $v_{ss_{nhb}}(s)$ , whose coefficients for node points are obtained by binomial expansion. For instance, considering a neighbourhood of  $n_{nhb} = 5$ , it is defined as follows:

$$v_{ss_{nhb}}(s) = -v_{i-2} + 4v_{i-1} - 6v_i + 4v_{i+1} - v_{i+2} \quad (2)$$

Thus, internal energy is defined as

$$E_{int} = \alpha(s)|v_s(s)|^2 + \beta(s)|v_{ss}(s)|^2 + \gamma(s)|v_{ss_{nhb}}(s)|^2 \quad (3)$$

With regards to the external forces, it is necessary to clarify that the proposed model works over two images at once: the first one ( $I$ ) is the original image after smoothing and augmenting contrast, while the second one ( $I'$ ) is the result of a more aggressive enhancement process, based on median filtering. This allows different levels of information to be taken into account at once during the process. Figure 5 shows a sample image and those processed to be used in the active contour-based process.

Considering both images, external energy  $E_{ext}$  is computed over them as follows:

$$E_{ext} = E_{ext}(I) + E_{ext}(I') \quad (4)$$

The particular energy terms extracted from each image capture information of intensity and edges. For a given image  $J$ , the intensity  $J_i$  at the current pixel is considered. Also, the intensity of the area above (or below) is included in a term  $J_{gi}$ . This term is obtained as follows: firstly, addition of pixel intensities above (or below) each pixel in the image is calculated; then, pixels with highest/lowest value in the region are searched and the gradient distance is computed over them.

Thus, the contour will be attracted to those pixels with the brightest/darkest region above (or below).

Information on edges is reflected as follows: an edge functional  $J_e$  is extracted using Sobel algorithm with non-maximum suppression and also the gradient distance  $J_g$ . Depending on the boundary, edges corresponding to light-to-dark or dark-to-light transitions are considered. Finally, an additional term  $J_{maxg}$  representing the distance between a node and the strongest edge in the area of searching is included.

Once all energy terms have been described, external energy for each of these images is presented in Equations (5) and (6) (note that some energy terms are only extracted from one of the two images). In these expressions, parameters  $u_1$  and  $u_2$  govern terms in  $E_{ext}(I)$ , whereas  $w_1$ ,  $w_2$ ,  $w_3$  and  $w_4$  control terms defining  $E_{ext}(I')$ .

$$E_{ext}(I) = u_1 I_i + u_2 I_g \quad (5)$$

$$E_{ext}(I') = w_1 I'_{gi} + w_2 I'_g + w_3 I'_e + w_4 I'_{maxg} \quad (6)$$

The active contour configuration depends on the boundary of interest. Internal energy terms, as well as information on edges, are used in the segmentation of all boundaries. Edges associated with dark-to-light transitions are considered for ILM, M/E and I/RPE, while light-to-dark ones are used in RPE/C segmentation. Regions with light intensities below are encouraged to segment M/E and RPE/C, while dark intensity above is considered only in M/E. For ILM, an additional term  $I_t$  is included in the definition of the external energy to encourage areas located at the top of image regarding those located at bottom. This term, governed by  $\epsilon$ , considers the row where the pixels is located as energy function. Thus, it will take low values for pixels located on the top part of the image and it would be greater for pixels that occupy rows near the bottom edge of the image.

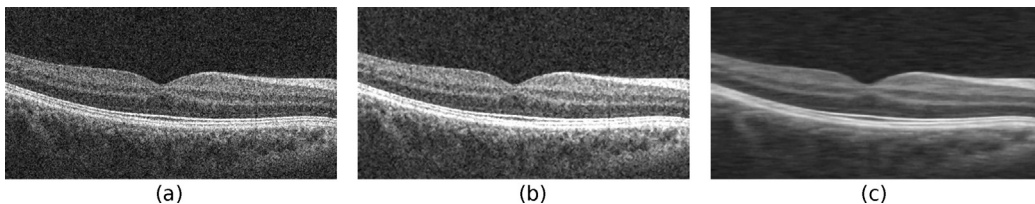


**Fig. 5 – Images used in the proposed active contour model: (a) sample original image; (b) first image, resulting of augmenting contrast; (c) second image, resulting of aggressive enhancement process (median filter with kernel size of  $19 \times 3$ ).**

Segmentation is obtained through  $n_s$  steps of active contour adjustment, depending on the boundary. These steps allows parameters to be adjusted dynamically, as a function of the information that must be considered. External energy is usually more predominant at the beginning, to attract the contour to the desired features, while internal energy typically increases in the final steps.

Regarding ILM,  $n_s = 3$ . Thus, external energy governs the process at the initial step; then, internal energy is increased and finally, more nodes are added to segment the fovea accurately.

For RPE/C,  $n_s = 2$ . Thus, after a coarse detection, a more refined adjustment is done. M/E requires  $n_s = 4$  steps: the process is governed by external energy and then, internal energy increases; after considering more nodes in the foveal area, final adjustment is done. Regarding I/RPE, only one step of adjustment is needed.

After the active contour-based process, final node points are interpolated to obtain the entire boundary. In Fig. 6, the process is applied over a sample image to segment RPE/C; some of the external energy terms taken into account are also presented.

Although this method obtains appropriate results, some critical situations should be taken into account, such as the presence of vessel shades, which appear when a cross-section of a vessel is present in the OCT image. The absorption of light

by the blood vessel walls causes vessel silhouettes to appear below the position of the vessel. These silhouettes or shades makes segmentation more complicated, especially for M/E boundary. This is due to the fact that, when this boundary is segmented, regions with dark intensity above are encouraged. Therefore, when a vessel shade is present, this information is misleading and nodes are attracted to wrong areas, as Fig. 7 presents. In order to avoid that, vessel shades should be detected to exclude influence of this intensity-based energy term in the active-contour evolution. A coarse detection of these structures is proposed in the text that follows. Thus, the segmentation process is designed to provide appropriate results even when these kind of structures are present.

**3.1.2.1. Detection of vessel shades.** The presence of vessel shades is determined by vertical regions along the image where the intensity changes to lower values suddenly, as Fig. 7(a) shows. Detecting these structures accurately would be hard, but in this work a coarse detection is proposed, with the purpose of excluding columns where they are present from the computation of the external energy term encouraging dark regions used to segment M/E boundary. This detection is based on detecting abrupt intensity changes along the columns in the image. Thus, mean intensity along each image column  $c$  is obtained, building a vector  $vec$ . Since M/E segmentation is performed after detecting ILM and RPE/C,

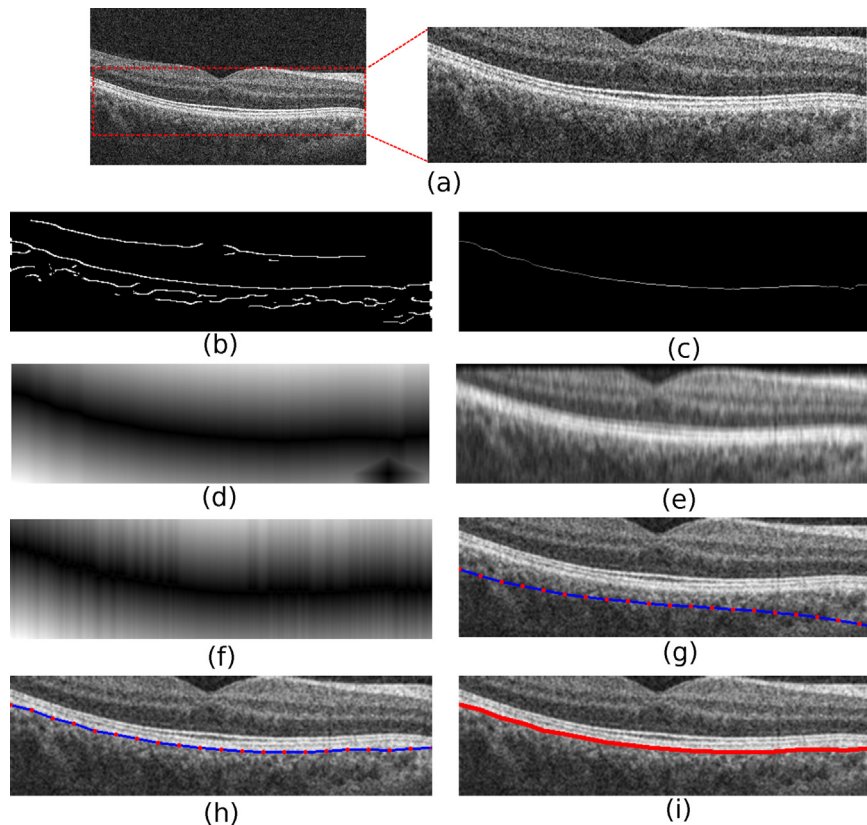


**Fig. 6 – Segmentation of RPE/C:** (a) original image where the rectangle identifies the ROI after the preprocessing; some energy terms: (b) edges (dark-to-light transitions); (c) best edge per column; (d) gradient distance over (c); (e) accumulated intensities above; (f) gradient distance over best pixel per column in (e); (g) initial active contour; (h) final configuration; (i) boundary as result of interpolating nodes.

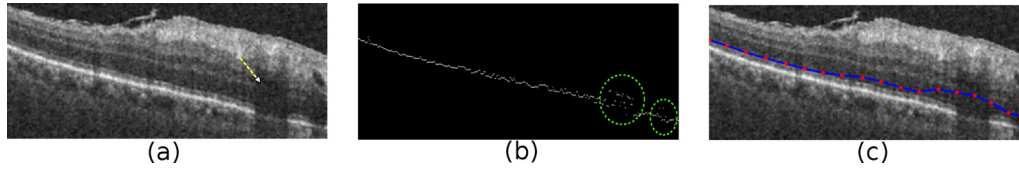


**Fig. 7 – Influence of the intensity-based energy term when a vessel shade is present: (a) sample image, with a vessel shade indicated by an arrow; (b) best pixel per column (with “goodness” as the lowest intensity above), marking misleading regions with circles; (c) active contour during process of M/E segmentation: nodes are attracted to wrong areas.**

computation of  $vec$  is done considering only information between these both boundaries. In order to smooth the data, this vector is blurred. Then, its median value  $vec_{med}$  is computed. This process is reflected graphically in Fig. 8. With this information, function  $vessel$  is defined to determine if column  $c$  corresponds to a vessel shade in the image:

$$vessel(c) = \begin{cases} 1 & \text{if } vec_c < (vec_{med} - 1.5 * vec_{std}) \\ 0 & \text{otherwise} \end{cases} \quad (7)$$

where  $vec_c$  is the value taken by  $vec$  at column  $c$ , whereas  $vec_{std}$  is the standard deviation computed over this vector. Therefore, a column is considered as vessel if its smoothed mean intensity is too far from the median value of the data. Thus, the threshold is established automatically for the particular conditions of each image.

When a column is marked as vessel shade, the energy term encouraging dark intensity above ( $J_{gi}$ , defined in Section 3.1.2) is not included in the computation of the external energy of a node. Thus, situations in which misleading regions attract a node are avoided. Figure 9 shows sample presented previously in Fig. 7 after excluding information of columns marked as vessels, obtaining an appropriate evolution of the active contour.

### 3.1.3. Refinement

As indicated above, information in the image is sometimes misleading, caused by presence of alterations or absence of information, causing inaccurate segmentation for some boundaries. In this section, process of refinement described in (González-López, Ortega, Penedo, & Charlón, 2014) for M/E and then, I/RPE and RPE/C simultaneously, are proposed in order to ensure the appropriate results.

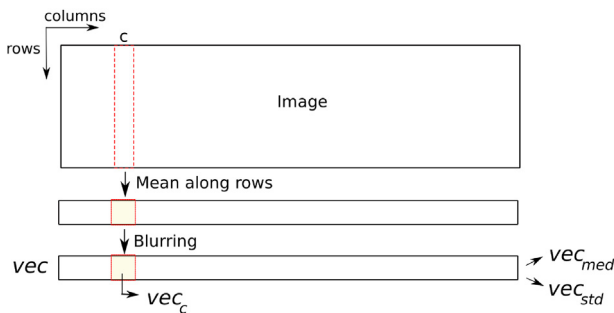


**Fig. 8 – Schema to obtain vector  $vec$ , useful to determine if a column can be marked as vessel shade.**

3.1.3.1. *Refinement of M/E.* Though M/E segmentation provides good accurate results, when the EZPR presents alterations, information in this area is lower and the active contour tends to segment I/RPE instead of M/E. Figure 10(a) presents a sample of unsuitable M/E segmentation caused by this situation. Therefore, a new energy-minimisation process to detect M/E is proposed to correct these results. Thus, when the previous segmented boundary is close enough to the I/RPE boundary, the new contour is initialised some pixels above and a process with  $n_s = 2$  steps is performed, since the current boundary is already near its real position. Different constraints from those considered in the initial segmentation are included in the energy terms used in this process. In this process, very low values of energy are considered when a node falls in an edge in the image, while strict internal constraints are kept. Therefore, the contour is very sensitive to presence of edges, which are used as clues of the presence of the boundary. On the other hand, when any edge cannot be detected in a region, internal constraints force nodes in this region to maintain continuity marked by the other ones (evidently, always when the region was not too wide).

Figure 10 (b) shows result of this process over unsuitable segmented boundary in (a). As can be observed, segmentation is corrected.

3.1.3.2. *Refinement of I/RPE and RPE/C.* A simultaneous refinement is proposed for I/RPE and RPE/C by taking advantage of the relationship between them. Since these boundaries can be assumed to be parallel (they are the limits of the same layer), the purpose of this step is to find a 3-degree parametric polynomial that fits both layer boundaries. To do that, a set  $C$  of curves is built, defined by all combinations of  $nc_{min}$  points corresponding to nodes in the active contour previously used to segment I/RPE. Each curve is evaluated as follows: distance between each node from I/RPE and point in the curve in the same column is computed. Then, the curve is displaced and its projection  $c'$  over each node in the RPE/C boundary can be obtained; thus, distance between them is computed too.

Fitness measure (number of nodes falling in the curve) is defined as the distance  $d_{cn_i}$  between the curve  $c$  and a node  $n_i$  (considering a neighbourhood  $M_i$ ):

$$d_{cn_i} = \begin{cases} 0 & \text{if } \exists m \in M_i | m \in c \\ 1 & \text{otherwise} \end{cases} \quad (8)$$

Therefore, the distance  $d_{cl}$  between a curve  $c \in C$  and a layer boundary  $l$  is defined as the accumulated distance to each of its nodes. Thus, distance  $d_g$  between a curve and both considered boundaries is given by

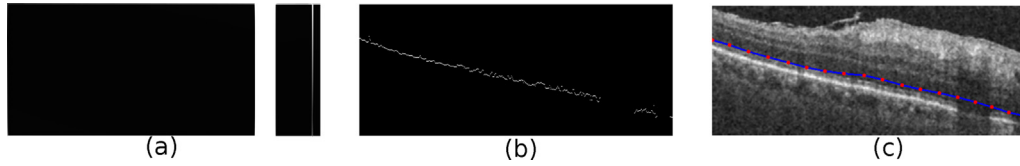


Fig. 9 – Influence of the intensity-based energy term after excluding vessel shades: (a) mask representing columns marked as vessels in white; (b) best pixel per column (with “goodness” as the lowest intensity above) after excluding those columns marked as vessel shades; (c) active contour during process of M/E segmentation: misleading information provided by the vessel shade is avoided.

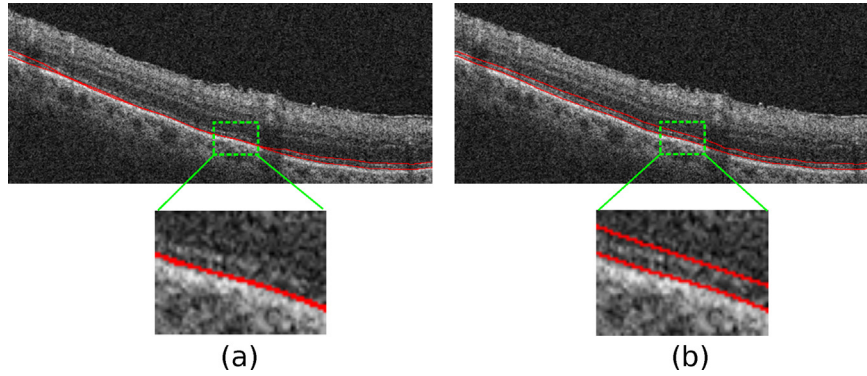


Fig. 10 – Refinement of M/E over a sample image: (a) zoomed unsuccessful segmentation of M/E, caused by the altered EZPR; (b) result after refinement process applied over (a).

$$d_g = d_{c_{I/RPE}} + \min(d_{c'_{I/RPE/C}}), r = 1 \dots m_{ci} \quad (9)$$

where  $d_{c_{I/RPE}}$  represents the distance to I/RPE boundary and  $d_{c'_{I/RPE/C}}$  that existing between the projection  $c'$  and the RPE/C boundary. It is necessary to consider that  $c'$  is obtained considering a range of rows  $m_{ci}$  around the each node in RPE/C, exploring all possible positions of the curve in order to find that which maximises the fitness measure. This process is reflected graphically in Fig. 11.

Thus, it is possible to determine that the searched curve  $c \in C$  is that which minimises the distance  $d_g$  to both boundaries, following Equation (10). Once the curve  $c$  is obtained, it replaces M/E and RPE/C, taking into account the appropriate displacement for each of these boundaries.

$$\operatorname{argmin}_k d g_k, \quad k = 1 \dots |C| \quad (10)$$

The results of this process over a sample image are presented in Fig. 12: (a) shows the final configuration of the active contour used to segment I/RPE and RPE/C, whose nodes at the end of the process are marked with small circles. It is possible

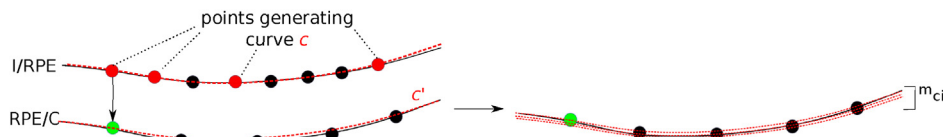


Fig. 11 – Curve projection over RPE/C: nodes in I/RPE are used to generate each curve  $c$ , which is displaced over a node in RPE/C to obtain  $c'$ , covering row range  $m_{ci}$  around this boundary.

to observe that I/RPE segmentation presented some mistakes (areas surrounded by dot-circles), tending to M/E or RPE/C. Contour nodes represented by big circles are those generating the best curve representing both I/RPE and RPE/C boundaries. This curve replaces their original segmentation, as Fig. 12 (b) shows, involving an evident improvement.

Once the method to detect the desired boundaries is known, it is possible to establish an area of interest in the retinal structure to perform the statistical information extraction.

### 3.2. Statistical computation service

Once the layer boundaries selected by the user are segmented over the whole OCT cube, the user can compute several statistical measures over the retinal volume determined by them. In a synthetic way, processes performed by this service are the following: the volume to be studied in the retina is bounded, based on the previously segmented layer boundaries; then, several statistics are extracted and finally, visual results are presented to the user.



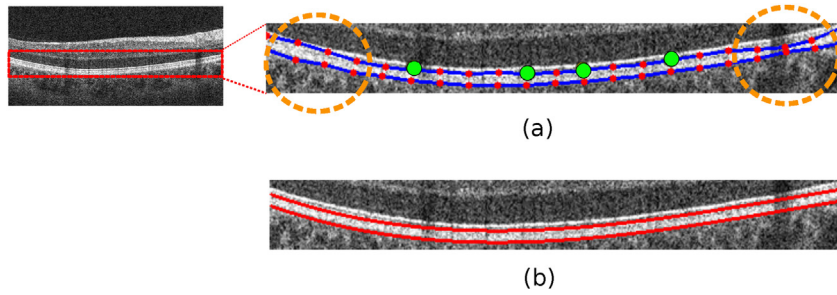


**Fig. 12 – Refinement for I/RPE and RPE/C: (a) Zoomed image, with the nodes obtained after segmenting I/RPE and RPE/C (small points) and those used as control points generating the best curve (big ones); dot-circles indicate areas where segmentation should be improved; (b) Result after replacing each boundary with that curve.**

### 3.2.1. Determining volume of interest

Although the Layer Segmentation Service (Section 3.1) provides the layer boundaries determining the retinal volume to be studied, sometimes the user needs a more flexible approach, bounding or further expanding the region to consider, depending on the research purposes. With that aim, the framework allows the user to modify the current boundary location, displacing it some pixels above or below its original position in the images. Thus, the area of interest in each image is modified and, consequently, the volume in the OCT cube to be processed.

### 3.2.2. Extracting statistical indicators

Once the retinal area at each image is bounded, information can be extracted. Since the idea is to build a map with the information for the entire retinal volume, all the OCT cube is considered. To do that, every image in the OCT sequence is explored, computing the statistical indicators as follows:

1. Fit the lower boundary to a curve.
2. For each point  $p$  at the fitting curve, obtain the normal line to the curve.
3. Find the intersection  $q$  of the normal with the upper boundary.
4. Compute the statistical measures over the pixels falling in the segment defined by  $p$  and  $q$ .

Thus, applying these steps to an OCT cube of  $z$  images with  $x$  columns and  $y$  rows, a set of  $z \times x$  values are obtained. Taking the curve that fits the bottom boundary in all images as baseline, a projection of all these values on  $x$ - $z$  coordinate plane can be built (see Fig. 13). In this work, mean and

standard deviation of the intensity distribution are considered as indicators, as well as the thickness of the studied area. Obviously, more measures can be included in the future.

### 3.2.3. Visualising results

After computing the statistical measures over all images in the OCT cube, results must be presented to the user. Since the OCT images are sampled scans from the retinal volume, the number of images  $z$  is usually lower than the image width  $x$ . In order to represent the information relating to the OCT cube in a consistent way, data are normalised and replicated in order to build a colour square-shaped map of side  $x$ , shown graphically in Fig. 13.

Besides the colour map, the ETDRS Grid (ETDRS Research Group, 1991) is also calculated. This grid is a widely used standard in the ophthalmic field because it allows information about the retina to be represented in a very condensed, easy-to-understand way. It is composed of three concentric circles, with the outer two divided into quadrants, which makes a total of nine sectors. For grid extraction, the optic disk and fovea location are needed, because the grid must be calculated taking as reference the line between both points (it will correspond to angle 0). Thus, quadrants considered in the grid will be obtained as a result of rotating the image  $d$  degrees from the baseline established by them. In order to obtain these points, the fundus image provided by the OCT device is taken as reference. Regarding the optic disk, the framework allows the user to mark its location on a fundus image. On the other hand, since the OCT images are captured centred on fovea, its location is given by the intersection of the reference lines on the fundus image. Thus, a procedure was designed and integrated in the framework to detect this point automatically.

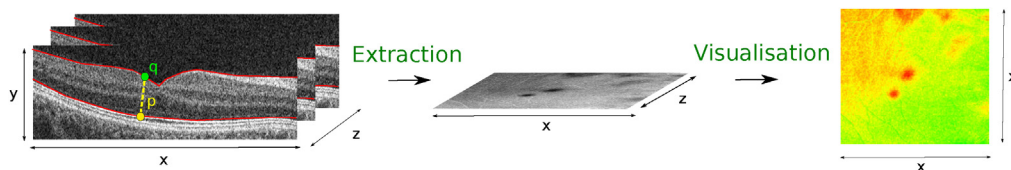


**Fig. 13 – Process of statistics extraction and visual results presented to the user: for each point  $p$  in the curve that fits bottom boundary, the normal is calculated and the intersection point  $q$  with the upper boundary determines the segment over which the statistics will be extracted; when this process is applied over the  $x$  columns for the  $z$  images, a map with indicator values can be built; finally, the map is processed to provide a suitable visualisation.**



**Table 1 – Values for initial parameters used in the active contour to segment ILM, RPE/C, M/E, I/RPE and refine M/E (M/E Ref).**

	ILM	RPE/C	M/E	I/RPE	M/E Ref
$n_{ac}$	26	21	18	25	21
$\alpha$	0.0001	0.05	0	0	0
$\beta$	0.0001	0.001	0	0.0001	0
$\gamma$	0.0001	0.0001	0.0001	0.0001	0.0001
$u_1$	0	0	0	0	0
$u_2$	0	0	0	0.001	0.001
$w_1$	0	0.1	0.05	0	0.001
$w_2$	0.001	0	0.001	0.01	0.01
$w_3$	−0.01	−0.01	0	0	0
$w_4$	0.1	0.01	0	0.001	0.001
$\varepsilon$	0.001	0	0	0	0

pixel size is  $11.98 \times 4.18 \mu\text{m}$ . Therefore, there is more information condensed at each pixel than in other works, which allows the robustness of the method to be evaluated in more challenging conditions. Image sides are not considered in the validation (Chiu et al., 2010), excluding 10% of the image width from either side of each image to avoid including regions with low signal. In these experiments, images have been analysed without considering information from adjacent frames in the sequence. This is a possibility to be tackled in the future, after frame alignment.

Parameters have been extracted empirically and they are presented in the text that follows. The neighbourhood in which a node can move is  $w_n \times h_n = 3 \times 3$  pixels. Regarding the second image used in the active contour-based process, it is processed using a median filter with kernel size  $k_x \times k_y = 19 \times 3$ . Table 1 shows parametrisation for initial active contours used in the segmentation: number of nodes ( $n_{ac}$ ) and weights for the different energy terms. Term  $n_{nhb}$  is set to 5 and in the I/RPE and RPE/C simultaneous refinement,  $n_{Cmin} = 4$ .

Two experiments have been designed to evaluate the proposed method. Firstly, the set of 5120 images were checked by an ophthalmologic expert to indicate if each boundary has

been segmented successfully or not. Thus, a qualitative measure of the segmentation obtained with the method is obtained, showing the clinical feasibility of the method considering a significant sample size. The aim of the second experiment was to provide a quantitative measure for the method. Therefore, results provided by the method are compared with those marked manually by the expert. Since the set of images is too big to be segmented in a manual way, in this experiment a subset of 56 images was considered.

## 4.2. Experiment I

In order to establish the feasibility of the method in the daily clinical practice, the proposed method was assessed over a large dataset (5120 images). Using the presented framework, the expert has checked all boundaries in each image to mark if they have been successfully segmented. Figure 16 shows samples of the segmented images presented to the expert, where (a) are images classified as correctly segmented by the expert, whereas (b) shows boundaries found to be unsuccessfully segmented (an arrow indicates those areas marked by the expert as mistaken). Thus, not only the percent of successfully/not successfully segmented boundaries in the dataset can be obtained (presented in Table 2) but also the situations in which the method may fail can be studied.

### 4.2.1. Discussion

Segmentation obtained by the current method can be appreciated on Fig. 16. Despite the high visual-quality results, boundaries marked as unsuccessful results in (b) allows the situations where the current method can present mistakes to be determined. Firstly, if RPE layer has many oscillations, a 3-degree curve can be insufficient to represent the shape of both its boundaries (I/RPE and RPE/C). However, this could be resolved by studying higher degree-polynomials to perform the process of refinement (although the main difficulty of this option is controlling the exact number of degrees of freedom that should be considered). On the other hand, it was observed that M/E refinement can present small deviations on both

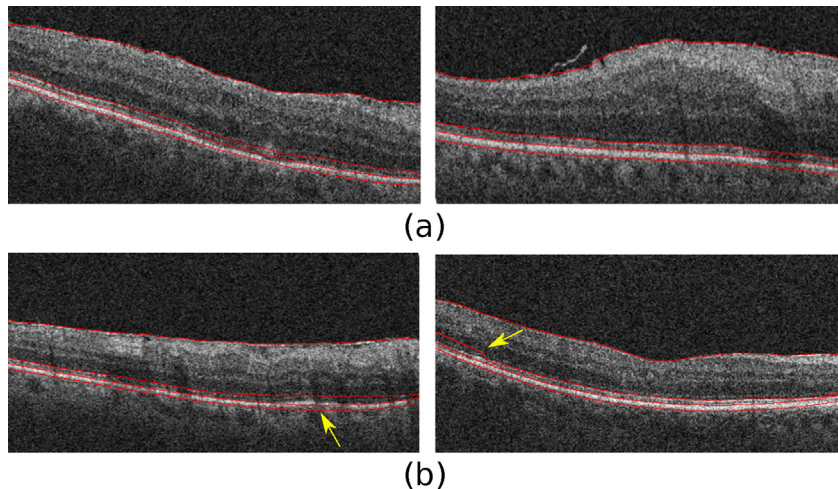


**Fig. 16 – Sample images with boundaries segmented by the proposed method: (a) images marked as successfully segmented by the expert; (b) images where the expert found some mistakes (indicated by an arrow).**



**Table 2 – Success rates obtained by the method presented in this work over a set of 5120 images. First row shows number of images segmented successfully or not (S/NS), while the second row shows the corresponding success rate (percent of images with successful segmentation).**

Boundary	ILM	M/E	I/RPE	RPE/C
S/NS	5118/2	4979/141	4581/539	4738/382
Success rate(%)	99.96	97.24	89.47	92.54

sides of the image when the signal is low, due to the high weight assigned to the edges in the process, and this could be revised in the future.

Once the kind of mistakes made by the method are known, the frequency of their occurrence can be observed in [Table 2](#), which shows the percent of images marked by the expert as successfully segmented (for each boundary). Best rates are obtained for ILM and M/E, with results for RPE/C slightly lower. Most of mistakes were made in I/RPE segmentation, which was expected, since it is the most difficult boundary to segment and its presence is not always immediately obvious, even to an expert. These results confirm the high effectiveness of the method. Though this experiment is useful to show that the method obtains appropriate results in qualitative terms, a quantitative assessment must be done. Therefore, that study is tackled in next section.

#### 4.3. Experiment II

Although the qualitative results presented in the previous experiment are promising, a quantitative study of results must be tackled. In this experiment, a subset of 56 images were extracted randomly from the original set, but respecting the distribution of mistakes calculated in the previous experiment. In this set, 35 images correspond to healthy

retinas, while the other 21 belong to pathological patients. The expert has marked manually the boundaries over the images using the application. Thus, differences between those marks and boundaries segmented with the automatic procedure can be computed. To do that, at each A-scan in the images, the difference between the boundary position of the method and the manual segmentation was calculated. Then, both signed and unsigned differences were averaged across all A-scans and images. Results in terms of mean and standard deviation in pixels are presented in [Table 3](#), where (a) and (b) present the differences computed over the images corresponding to healthy and pathological retinas, respectively. [Table 4](#) (a) summarises the results over all 56 images.

Though comparison with the state-of-the-art layer segmentation methods would be desirable, results for active contour-based methods are not available. Therefore, methods based on other approaches are considered and the comparison is developed in two ways: firstly, a graph-based method is evaluated over the same dataset, in order to make a consistent comparison; then, results provided by other state-of-the-art methods are shown, with the purpose of determining if the performance of the proposed method is appropriate.

The graph-based method used by [González, Ortigueira, Ortega, and Penedo \(2014\)](#), which is a derivation of the work developed by [Haeker et al. \(2007\)](#), tackles the segmentation of ILM and RPE/C boundaries with a pyramidal approach and can be applied over this set of images. Then, differences between results using that approach and the delimitation made by the expert are computed and shown in [Table 4](#) (b).

Regarding the other considered methods in the field, those chosen were from [Lee et al. \(2010\)](#) and [Kafieh et al. \(2013\)](#), who consider graph-based methods and [Yang et al. \(2011\)](#), whose method is based on gradient and shortest path. A dataset containing images from glaucomatous patients was used to assess the method proposed by [Kafieh et al. \(2013\)](#) and [Lee et al. \(2010\)](#). [Yang et al. \(2011\)](#) considered images from

**Table 3 – Signed and unsigned differences between boundaries segmented using the proposed method and those marked manually by the expert, in terms of mean  $\pm$  std in pixels, computed over images correspondent to (a) healthy and (b) pathological retinas, respectively.**

	ILM	M/E	I/RPE	RPE/C	Overall
(a) Healthy (35 images)					
Signed	0.46 $\pm$ 1.84	0.60 $\pm$ 1.87	−0.11 $\pm$ 1.43	0.61 $\pm$ 1.90	−0.23 $\pm$ 1.58
Unsigned	1.23 $\pm$ 1.45	1.29 $\pm$ 1.48	0.78 $\pm$ 1.20	1.29 $\pm$ 1.52	1.07 $\pm$ 1.28
(b) Pathological (21 images)					
Signed	0.10 $\pm$ 1.64	0.32 $\pm$ 1.29	−1.13 $\pm$ 1.83	−0.20 $\pm$ 1.55	0.39 $\pm$ 1.76
Unsigned	1.02 $\pm$ 1.29	0.79 $\pm$ 1.06	1.44 $\pm$ 1.60	1.03 $\pm$ 1.18	1.15 $\pm$ 1.41

**Table 4 – Signed and unsigned differences between boundaries segmented over the subset of 56 images using the automatic method and those marked manually by the expert, in terms of mean  $\pm$  std in pixels: (a) Results for the proposed method; (b) Results obtained using the graph-based approach (only available for ILM and RPE/C boundaries).**

	ILM	M/E	I/RPE	RPE/C	Overall
(a) Proposed method					
Signed	0.24 $\pm$ 1.73	0.43 $\pm$ 1.54	−0.75 $\pm$ 1.77	0.11 $\pm$ 1.73	0.005 $\pm$ 1.691
Unsigned	1.10 $\pm$ 1.35	0.98 $\pm$ 1.26	1.19 $\pm$ 1.50	1.13 $\pm$ 1.32	1.10 $\pm$ 1.36
(b) Graph-based method					
Signed	−0.27 $\pm$ 1.84	–	–	−0.60 $\pm$ 1.64	−0.43 $\pm$ 1.74
Unsigned	1.16 $\pm$ 1.45	–	–	1.18 $\pm$ 1.29	1.17 $\pm$ 1.37



patients with retinitis pigmentosa. However, it is necessary to clarify that experiments were done in restricted conditions, such as excluding boundaries from the validation when the expert considered them as not visible. Our proposed method was validated considering entire boundaries (when information is not enough, it can provide good approach for the boundaries). The graph presented in Fig. 17 shows results (unsigned differences) obtained by these methods over the considered boundaries (except for I/RPE boundary, which are not available for these datasets).

#### 4.3.1. Discussion

Results shown in Table 3 shows that the proposed method provides similar results for the images corresponding to both patient groups (healthy and pathological). However, it is remarkable that it presents even higher accuracy for some boundaries on pathological images. This is due to the fact that it was designed and refined for this kind of situations, while it must maintain appropriate behaviour for the healthy ones.

With regards to the global results (computed over the 56 images), Table 4 (a) shows that the mean unsigned differences obtained for all boundaries are around one pixel, whereas the signed differences are less. When these results are compared to those obtained using the graph-based method, it is possible to observe that the proposed method presents higher accuracy for the available boundaries (ILM and RPE/C). Therefore, the method is more effective for this task.

Regarding Fig. 17, although a precise comparison is not easy, because each existing method considers different settings, this graph reflects that results at pixel level obtained by the proposed method are similar to previous works, and are better in most cases. Unsigned differences are low and also quite constant for all the studied boundaries. Although standard deviation is not high, comparison with other methods suggests that it could be improved.

These results indicate that the process performed for M/E, which seeks to detect overlapping boundaries in order to perform a more exhaustive process of segmentation, is appropriate. The low error obtained for I/RPE and RPE/C suggests that the refinement process is relevant to obtain a high

accuracy. In particular, results for I/RPE are remarkable, since it was not considered in the other experiments.

This proposal provides similar results to those obtained by the most recent methods. Besides that, it segments entire boundaries, without excluding any part (even when they are not evident), which is a very salient feature. That, in conjunction with results presented in the previous experiment, leads to the conclusion that this method provides accurate results in less controlled environments. Therefore, it would be feasible for ophthalmologist' daily clinical practice.

#### 4.4. Framework evaluation

The global framework presented in this work must be assessed from a research perspective. An experimental research was proposed by medical specialists with the aim of evaluating the correlation between the layer intensity distribution in the OCT retinal images and some kinds of pathologies. This study (Llano-Atanes, 2013), was performed in the Instituto Oftalmológico Gómez-Ulla (Santiago de Compostela), considering 73 images from 42 Caucasian patients. The study was focused on the retinal volume defined by ILM and M/E and, as statistics, the mean and standard deviation of the intensity distribution were considered. The statistics obtained from healthy patients were studied with the purpose of establishing standard values of normality. Thus, values extracted from patients with alterations, such as Cystoid Macular Edema (CME), could be correlated with the disease. In addition, experts also assessed the influence of the different experimental conditions to perform the study.

The framework presented in this work has made it possible for experts to tackle the study. Images were processed to delimit retinal layers automatically and then, indicators were computed and presented to the user in a friendly and easy-to-export format. In addition to the large amount of information that the application can provide to the experts in a very short time, it allows all computed results to be stored. Therefore, the ophthalmologists could filter the information of interest in relation to different criteria: patient age, pathology, etc. This functionality allowed particular results presented by the different groups of patients to be studied, ensuring the scope for research completeness.

Besides the useful clinical results obtained with the tool, since it is a web-oriented framework, the experts could access and extract all the information from their own work places. All these characteristics, apart from speeding up the research, made the application a very helpful tool for research purposes.

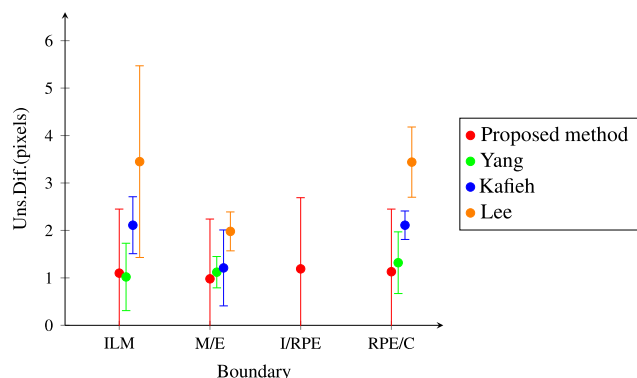


**Fig. 17 – Unsigned differences in pixels (mean  $\pm$  std) obtained for each boundary using proposed and state-of-the-art methods. Note that different datasets have been considered for testing and that results for I/RPE are not available for the rest of methods.**

## 5. Conclusions and future work

Image-based processing applications are essential in the medical field, since images are an important aspect in expert clinical practice. In ophthalmology, OCT images have become a standard in disease diagnosis because the retinal layers present in them provide much information to the experts. With the aim of designing an automatic framework to process OCT images and extracting relevant information from them that would be useful for ophthalmologists, different tools

have been proposed and integrated with a web interface. Thus, the application includes different modules, each one providing a particular service to the user, as well as a properly developed interface.

In particular, two services have been included in the application described in this work. The first one consists of a module to segment automatically the retinal layers in OCT images. This module implements a method based on active contours. Validation showed that this methodology is suitable for this task, since the obtained results were in line with those provided by methods in the state of the art.

The second service is focused on the extraction of statistical indicators from the retinal volume defined by these images. Information provided by the first service is used to bound the area in each image to be studied. Then, statistics are extracted from all images in the OCT cube in order to build maps representing information for all retina. Thus, they can be presented to the experts in a condensed and easy-to-understand way, allowing results to be exported in different formats, which is very useful for ophthalmic research.

Both services are available through a web interface to the experts, allowing these functionalities to be used in a distributed environment, encouraging collaboration between different centres. The proposed framework has been analysed and assessed in a real medical context with clinical and research functions. Although a study of usability has not been performed, in the experimental cases where the application was used, all the required properties were revised.

As future work, the described services can be extended in order to segment the rest of the layers in the retina, as well as providing more statistical indicators. Additional modules will be designed with the purpose of integrating new services into the application. The idea is that when new services to analyse medical images are demanded, new modules can be integrated in the framework easily to extend its capabilities.

## Acknowledgements

This paper has been partly funded by the Instituto de Salud Carlos III (Ministerio de Economía y Competitividad) under PI14/02161 project and the Secretaría de Estado de Investigación, Desarrollo e Innovación of the Spanish Government (A. González-López acknowledges its support under FPI Grant Program).

## REFERENCES

- Abràmoff, M., & Suttorp-Schulten, M. (2005). Web-based screening for diabetic retinopathy in a primary care population: the eyecheck project. *Telemedicine Journal and E-Health*, 11(10), 668–674.
- Albrecht, P., Ringelstein, M., Mueller, A., Keser, N., Dietlein, T., Lappas, A., et al. (2012). Degeneration of retinal layers in multiple sclerosis subtypes quantified by optical coherence tomography. *Multiple Sclerosis Journal*, 18(10), 1422–1429.
- Antony, B. J., Abràmoff, M. D., Lee, K., Sonkova, P., Gupta, P., Kwon, Y., et al. (2010). Automated 3d segmentation of intraretinal layers from optic nerve head optical coherence tomography images. In *SPIE Medical Imaging. International Society for Optics and Photonics*, 76260U-76260U.
- Blackledge, J., & Dubovitski, D. (2011). Mole test: a web-based skin cancer screening system. In *The Third International Conference on Resource Intensive Applications and Services* (Vol. 978-1-61208-006-2, pp. 22–29).
- Bowd, C., Weinreb, R., Williams, J., & Zangwill, L. (2000). The retinal nerve fiber layer thickness in ocular hypertensive, normal, and glaucomatous eyes with optical coherence tomography. *Archives of Ophthalmology*, 118(1), 22–26.
- Chiu, S. J., Li, X. T., Nicholas, P., Toth, C. A., Izatt, J. A., & Farsiu, S. (Aug 2010). Automatic segmentation of seven retinal layers in sdopt images congruent with expert manual segmentation. *Optics Express*, 18(18), 19413–19428.
- ETDRS Research Group. (1991). Etdrs report number 10: grading diabetic retinopathy from stereoscopic color fundus photographs—an extension of the modified airlie house classification. *Ophthalmology*, 98, 786–806.
- Garvin, M. K., Abràmoff, M. D., Wu, X., Russell, S. R., Burns, T. L., & Sonka, M. (2009). Automated 3-d intraretinal layer segmentation of macular spectral-domain optical coherence tomography images. *IEEE Transactions on Medical Imaging*, 28(9), 1436–1447.
- González-López, A., Ortega, M., Penedo, M., & Charlón, P. (2014). Automatic robust segmentation of retinal layers in oct images with refinement stages. In *International Conference on Image Analysis and Recognition – ICIAR 2014*. Vol. 8815 of *Lecture Notes in Computer Science* (pp. 337–349). Springer Berlin Heidelberg.
- González, A., Ortigueira, C., Ortega, M., & Penedo, M. (2014). Quantitative study on a multiscale approach for oct retinal layer segmentation. In *6th International Conference on Agents and Artificial Intelligence (ICAART 2014)* (Vol. 1, pp. 715–723).
- Haeker, M., Sonka, M., Kardonc, R., Shah, V. A., Wu, X., & Abràmoff, M. (2007). Automated segmentation of intraretinal layers from macular optical coherence tomography images. *Proceeding of SPIE: Medical Imaging*, 6512.
- Itoh, Y., Inoue, M., Rii, T., Hirota, K., & Hirakata, A. (2013). Correlation between foveal cone outer segment tips line and visual recovery after epiretinal membrane surgery. *Investigative Ophthalmology & Visual Science*.
- Kafieh, R., Rabbani, H., Abràmoff, M. D., & Sonka, M. (2013). Intra-retinal layer segmentation of 3d optical coherence tomography using coarse grained diffusion map. *Medical Image Analysis*, 17(8), 907–928.
- Karsch, K., Grinstead, B., He, Q., & Duan, Y. (2008). Web based brain volume calculation for magnetic resonance images. *Conference of the IEEE Engineering in Medicine and Biology Society*, 2008, 1210–1213.
- Kass, M., Witkin, A., & Terzopoulos, D. (1988). Snakes: active contour models. *International Journal of Computer Vision*, 1(4), 321–331.
- Keane, P. A., Patel, P. J., Liakopoulos, S., Heussen, F. M., Sadda, S. R., & Tufail, A. (2012). Evaluation of age-related macular degeneration with optical coherence tomography. *Survey of Ophthalmology*, 57(5), 389–414.
- Lee, K., Niemeijer, M., Garvin, M. K., Kwon, Y. H., Sonka, M., & Abràmoff, M. D. (2010). Segmentation of the optic disc in 3-d oct scans of the optic nerve head. *IEEE Transactions on Medical Imaging*, 29(1), 159–168.
- Llano-Atanes, R. (2013). Assessment of an automated tool for measuring layer contrast in oct retinal images (in spanish). Master's thesis. University of Santiago de Compostela.
- Mishra, A., Wong, A., Bizheva, K., & Clausi, D. A. (Dec 2009). Intra-retinal layer segmentation in optical coherence tomography images. *Optics Express*, 17(26), 23719–23728.
- Ortega, M., Barreira, N., Novo, J., Penedo, M. G., Pose-Reino, A., & Gómez-Ulla, F. (2010). Sirius: a web-based system for retinal image analysis. *International Journal of Medical Informatics*, 79(10), 722–732.

- Puzeyeva, O., Lam, W. C., Flanagan, J. G., Brent, M. H., Devenyi, R. G., Mandelcorn, M. S., et al. (2011). High-resolution optical coherence tomography retinal imaging: A case series illustrating potential and limitations. *Journal of Ophthalmology*.
- Sanchez-Tocino, H., Alvarez-Vidal, A., Maldonado, M. J., Moreno-Montañes, J., & Garcia-Layana, A. (2002). Retinal thickness study with optical coherence tomography in patients with diabetes. *Investigative Ophthalmology & Visual Science*, 43(5), 1588–1594.
- Shiono, A., Kogo, J., Klose, G., Takeda, H., Ueno, H., Tokuda, N., et al. (2013). Photoreceptor outer segment length: a prognostic factor for idiopathic epiretinal membrane surgery. *Ophthalmology*, 120(4), 788–794.
- Tian, T., Zhu, X.-H., & Liu, Y.-H. (2011). Potential role of retina as a biomarker for progression of parkinson's disease. *International Journal of Ophthalmology*, 4(4), 433–438.
- Yang, Q., Reisman, C. A., Chan, K., Ramachandran, R., Raza, A., & Hood, D. C. (Sep 2011). Automated segmentation of outer retinal layers in macular oct images of patients with retinitis pigmentosa. *Biomedical Optics Express*, 2(9), 2493–2503.
- Yaqoob, Z., Wu, J., & Yang, C. (2005). Spectral domain optical coherence tomography: a better oct imaging strategy. *Biotechniques*, 39(Suppl. 6), S6–S13.
- Yazdanpanah, A., Hamarneh, G., Smith, B. R., & Sarunic, M. (2011). Segmentation of intra-retinal layers from optical coherence tomography images using an active contour approach. *IEEE Transactions on Medical Imaging*, 30(2), 484–496.
- Yohannan, J., Bittencourt, M., Sepah, Y. J., Hatef, E., Sophie, R., Moradi, A., et al. (2013). Association of retinal sensitivity to integrity of photoreceptor inner/outer segment junction in patients with diabetic macular edema. *Ophthalmology*, 120(6), 1254–1261.